The Astrophysical Journal, 708:403–410, 2010 January 1 doi:10.1088/0004-637X/708/1/403

ABSOLUTE TIMING OF THE CRAB PULSAR WITH THE *INTEGRAL*/SPI TELESCOPE*,†

S. Molkov, E. Jourdain, and J. P. Roques
CESR-Universite de Toulouse (UPS), CNRS (UMR 5187), 9 Av. du Colonel Roche, 31028 Toulouse Cedex 4, France; molkov@iki.rssi.ru
Received 2009 June 29; accepted 2009 November 5; published 2009 December 11

ABSTRACT

We have investigated the pulse shape evolution of the Crab pulsar emission in the hard X-ray domain of the electromagnetic spectrum. In particular, we have studied the alignment of the Crab pulsar phase profiles measured in the hard X-rays and in other wavebands. To obtain the hard X-ray pulse profiles, we have used six years (2003–2009, with a total exposure of about 4 Ms) of publicly available data of the SPI telescope on-board the *International Gamma-Ray Astrophysics Laboratory* observatory, folded with the pulsar time solution derived from the Jodrell Bank Crab Pulsar Monthly Ephemeris. We found that the main pulse in the hard X-ray 20–100 keV energy band leads the radio one by 8.18 ± 0.46 milliperiods in phase, or 275 ± 15 μs in time. Quoted errors represent only statistical uncertainties. Our systematic error is estimated to be $\sim$40 μs and is mainly caused by the radio measurement uncertainties. In hard X-rays, the average distance between the main pulse and interpulse on the phase plane is 0.3989 ± 0.0009. To compare our findings in hard X-rays with the soft 2–20 keV X-ray band, we have used data of quasi-simultaneous Crab observations with the proportional counter array monitor on-board the *Rossi X-Ray Timing Explorer* mission. The time lag and the pulses separation values measured in the 3–20 keV band are 0.00933 ± 0.00016 (corresponding to 310 ± 6 μs) and 0.40016 ± 0.00028 parts of the cycle, respectively. While the pulse separation values measured in soft X-rays and hard X-rays agree, the time lags are statistically different. Additional analysis show that the delay between the radio and X-ray signals varies with energy in the 2–300 keV energy range. We explain such a behavior as due to the superposition of two independent components responsible for the Crab pulsed emission in this energy band.

Key words: pulsars: general – pulsars: individual (PSR B0531+21) – stars: neutron – X-rays: stars

Online-only material: color figures

1. INTRODUCTION

The Crab pulsar (PSR B0531+21) is the best studied isolated pulsar. The pulsed emission was discovered long ago and in the X-rays (Fritz et al. 1969; Bradt et al. 1969) and in the γ-rays (Kurfess 1971) domains. and its pulse morphology has been studied in the full range of the electromagnetic spectrum. In all energies, the pulse profile has two prominent features, the main pulse (or the first peak, P1) and the interpulse (or the second peak, P2). The relative intensities of these peaks depend on the energy band. The second peak dominates in the $\sim$200–1200 keV energy band. By all appearances, the distance between the peaks on the phase plane is almost constant in time, slightly varying around the value $\Delta\psi = 0.40(0)$ depending on energy (see Thompson et al. 1977; Wills et al. 1982; White et al. 1985; Nolan et al. 1993; Masnou et al. 1994; Moffett & Hankins 1996; Pravdo et al. 1997; Kuiper et al. 2001; Brandt et al. 2003; Rots et al. 2004; The MAGIC Collaboration 2008). For a long time it has been assumed that both peaks are perfectly lined up in phase over the whole energy range. This assumption has been disputed for the first time in the work of Masnou et al. (1994). Based on the data of the FIGARO II telescope (balloon experiment), the authors found that the first peak in the 0.15–4 MeV energy band leads the radio main pulse by $\sim 400 \pm 150$ μs. Later, the misalignment in phase of the main radio pulse and the main pulse in shorter wavelengths has been confirmed by several instruments. No absolute agreement exists in the value of the radio delay measured by different instruments even for the same energy band, though they are close to each other especially if one takes into account not only statistical errors but also the possible systematic uncertainties. The most recent measurements of the X-,γ-rays to radio lag are *Rossi X-ray Timing Explorer* (*RXTE*)/lproportional counter array (PCA)—344 ± 40 μs (Rots et al. 2004), JEM-X/*International Gamma-Ray Astrophysics Laboratory* (*INTEGRAL*)—300 ± 67 μs (Brandt et al. 2003), ISGRI/ and SPI/*INTEGRAL*—285 ± 12 μs and 265 ± 23 μs, respectively (statistical errors only; Kuiper et al. 2003), EGRET/*Compton Gamma Ray Observatory* (*CGRO*)—241 ± 29 μs (Kuiper et al. 2003). The *INTEGRAL* results mentioned above are based on observations covering only several days, thus these data can be folded with the single ephemeris record, while different ephemerides were used for *RXTE* and *CGRO* observations. This means that *RXTE* and *CGRO* results should be statistically more significant since they are less affected by uncertainties in the radio ephemerides (see Rots et al. 2004). Recently, the optical-radio delay has also been confirmed, 255 ± 21 μs (Oosterbroek et al. 2008).

In this paper, we present the timing analysis of the Crab pulsar in the 2–300 keV energy range with the SPI/*INTEGRAL* telescope and the *RXTE* instruments.

2. OBSERVATIONS AND DATA REDUCTION

2.1. *INTEGRAL*

The INTEGRAL (Winkler et al. 2003) was launched on Proton/Block-DM on 2002 October 17 into a geosynchronous highly eccentric orbit with high perigee (Eismont et al. 2003). The scientific payload of *INTEGRAL* includes four telescopes: the spectrometer SPI (Vedrenne et al. 2003), the imager

* Based on observations with *INTEGRAL*, an ESA project with Instruments and Science Data Center funded by ESA member states (especially the PI countries: Denmark, France, Germany, Italy, Switzerland, Spain), Czech Republic and Poland, and with the participation of Russia and the USA.
† http://www.jb.man.ac.uk

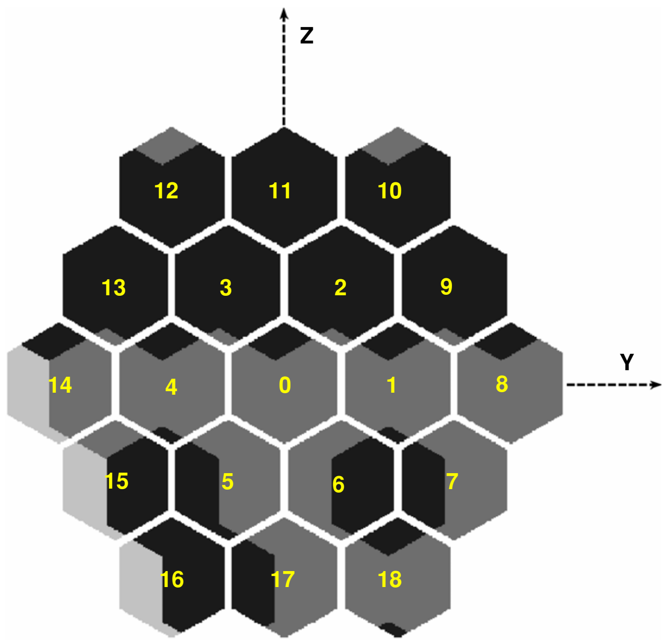

Figure 1. Shadowgram of the detectors plane of the SPI telescope in the simple case when only one source is located in the SPI FOV. The"black" color corresponds to the area illuminated by the source; "dark gray" to the area shadowed by the mask; "light gray" to the area closed for the source by the collimator.

IBIS (Ubertini et al. 2003), the X-ray monitor JEM-X (Lund et al. 2003), and the optical monitor OMC (Mas-Hesse et al. 2003).

2.1.1. The SPI Telescope Characteristics

In this paper, we focus on analysis of the SPI data. For detailed description of the instrument calibrations and performance, see Vedrenne et al. (2003), Attié et al. (2003), and Roques et al. (2003). Below we give only a brief review of the key characteristics of the instrument and software relevant for this work.

SPI consists of 19 high purity germanium detectors (GeD) packed into a hexagonal array (see Figure 1). The combination of a good sensitivity to the continuum and line emission in the energy band 20–8000 keV, provided by a large geometrical detector's plane area ($\sim$500 cm^2) and cryogenic system, and a good timing resolution (102.4 μs) gives us an opportunity to study even very fast X/γ-rays pulsars.

There are two main types of SPI events: single events (registered by only one detector) and multiple events (scattered photon detected by two and more detectors). Though the pulsating signal is clearly detected in both types of events, we did not use the multiple events because of difficulties in the extraction of the spatial information, worse timing resolution, and the lack of a tested energy response matrix. It should be noted that this kind of data was successfully used by Dean et al. (2008) for measuring Crab polarization.

2.1.2. The SPI Clock and Time Connection

SPI has its own internal clock, a 20 MHz oscillator that generates time tag signal every 2048 periods, i.e., 102.4 μs—the time resolution of the instrument. The SPI clock is synchronized with the on-board clock at every 125 ms (the 8 Hz on-board cycle, $\mathrm{OBT_{8Hz}}$) by a resetting of the counter associated with the SPI oscillator. The SPI time tags are counted from the beginning of the 8 Hz cycle and divide the 125 ms interval into 1019 intervals of 102.4 μs duration plus one interval with a duration of 70 μs. In fact, the base frequencies of both on-board and SPI clocks are slightly varying with time (e.g., due to variation of the crystals temperature) that leads to variation in duration of SPI time tag intervals. We have estimated this effect to be very small (<5 μs for any statistically significant analysis), neglected it, and used the nominal values of the frequencies. The on-board time (OBT) of the current 8 Hz cycle is the value of the datation of the beginning of the cycle (SPI User Manual—Issue 5.2—SEP 2002). By convention, the OBT of any event is the time of the leading edge of the interval where the event has been detected, that is:

$$\mathrm{OBT} = \mathrm{OBT_{8Hz}} + N_{tt} * D/2^{-20}, \qquad (1)$$

where N_{tt} is the number of the SPI time tag interval (0, ..., 1019) and $D = 102.4 \times 10^{-6}$s is the length of the interval. The divisor 2^{-20} is introduced to convert time expressed in seconds to OBT units and reflects the conventional time resolution of the *INTEGRAL* clock (the real clock accuracy is 2^{-19} s). For the conversion of the OBT to Coordinated Universal Time (UTC) and for the barycentric correction we have used routines from the standard Off-line Science Analysis software package version 7.0 developed at *INTEGRAL* Science Data Centre (Courvoisier et al. 2003) and the time correlation files provided with the auxiliary data for the *INTEGRAL* data archive generation number 2. Equation (1) and the time transformation routines ensure accuracy of returning Universal Time of the order of 100 μs. For precise timing analysis, a time correction must be added to OBT before any conversion:

$$\Delta T = \Delta T_{\mathrm{SPI}} + \Delta T_{\mathrm{sat}} + \Delta T_{\mathrm{rev2}}, \qquad (2)$$

where $\Delta T_{\mathrm{SPI}} = D/2 = 51.2$ μs—the mean systematic shift due to the fact that the arrival time of events is defined as the time of the leading edge of the time tag interval, while the actual arrival times are normally distributed inside the time tag interval; $\Delta T_{\mathrm{sat}} = 83$ μs—the delay between the OBT and SPI time (ground calibration; Alenia Spazio 2002); $\Delta T_{\mathrm{rev2}} = -47$ μs—this shift is common for all time correlation files from the archive generation 2 (will disappear in the new generation of archive). Note, that the SPI instrumental delay given in Table 4 of Walter et al. (2003) is the sum of the first two terms (134 μs) of expression (2).

In our analysis, to avoid an additional discretization in time series we decided to define the time of any registered event not as the time of the leading edge of the appropriate time tag interval, but as a linearly randomized time inside this time tag interval, and the final expression for OBT is as follows:

$$\mathrm{OBT} = \mathrm{OBT_{8Hz}} + ((N_{tt} + \mathrm{rand}[0,1]) * D + \Delta T)/2^{-20}, \qquad (3)$$

in this case $\Delta T_{\mathrm{SPI}} = 0$ and therefore $\Delta T = +36 \times 10^{-6}$ s.

2.1.3. Data Selection

In our analysis, we have used publicly available data of all observations where the source was in the field of view (FOV) of the SPI telescope. The exposure of selected data totals up approximately 4 Ms (see Table 1).

SPI is a telescope with a coded mask aperture and most *INTEGRAL* observations are organized as a set of snapshots of the sky around a target (pointings or Science Windows, SCWs—continuous observations pointed on a given direction in the sky). It means that the instrument effective area for the chosen target is changing from pointing to pointing. This effective area is mainly determined by geometrical area of the non-shadowed part of the detector plane (see Figure 1).

To extract the Crab pulsed signal we have used the epoch folding technique (Leahy et al. 1983). Any set of observations can be represented as a set of the whole detector plane count rates and in these terms, the total folded curve is the direct sum of the folded countrates of the individual pointings. To reach the best result we need to find an optimal series of the *INTEGRAL* pointings for which the signal to noise ratio will be the highest one. In this regard, several parameters characterize each pointing: the exposure of the pointing, T_i; the background conditions—the instrumental background countrate plus the sum of the countrates from other sources in the FOV, C_i^b; the illumination fraction of the detector plane, α_i, corresponding to the source direction (could include not only geometrical factor, varies from 0 to ∼0.6); and the mean countrate of the pulsating part of the source emission, C_i^p (for completeness, below we are introducing also the term C_i^{dc}—the mean unpulsating countrate of the pulsar, for the Crab pulsar $C_i^{dc} = 0$). Using the terminology introduced above and assuming that all variances follow the Poisson statistic, the signal to noise ratio for the sequence of M pointings can be expressed as follows:

$$\left(\frac{S}{N}\right)_M = \frac{\sum_{i=1}^{M} \alpha_i C_i^p T_i}{\sqrt{\sum_{i=1}^{M} (C_i^b + \alpha_i (C_i^p + C_i^{dc})) T_i}}. \tag{4}$$

The optimal set of K pointings chosen from the initial set of M pointings is that for which the value of $(S/N)_K$ calculated using Equation (4) reaches its maximum. In the case of a large number M the exhaustive search will take infinite time (even for $M = 100$ the number of combinations exceeds 10^{30}, in our case $M > 1000$). Several simplifications have been investigated.

Considering that the *INTEGRAL* pointings (or SCWs) cover generally ∼2–5 ks time intervals, we can treat the exposure T_i of individual member of the data series as constant, i.e., $T_i \simeq \text{const} = T, i \in [1, M]$. Moreover, in the SPI telescope, the background dominates the useful signal, i.e., $(C_i^p + C_i^{dc}) \ll C_i^b$ is true for any point source excluding the brightest events like gamma-ray bursts or short intense bursts from soft gamma-ray repeaters and anomalous X-ray pulsars. Further, the amplitude of the variation of the SPI background does not exceed ∼50% of its mean level (excluding periods of Solar flares). So, we can treat $C_i^b \simeq \text{const} = C_b$ for $i \in [1, M]$. We assume also that the mean value of the pulsar "Pulsed" component is constant in time $C_i^p \simeq \text{const} = C_p$. Now, taking into account assumptions listed above, we can modify Equation (4) as

$$\left(\frac{S}{N}\right)_M \simeq \sqrt{\frac{T C_p^2}{C_b}} \frac{\sum_{i=1}^{M} \alpha_i}{\sqrt{M}}. \tag{5}$$

In Equation (5), we do not reduce the number of combinations in comparison with Equation (4) but now it is easy to see that the procedure of searching for the optimal set is equivalent to searching for the maximum value of the following discrete function:

$$F(K) = \frac{\sum_{i=1}^{K} \beta_i}{\sqrt{K}}, K \in [1, M], \tag{6}$$

where $B = [\beta_i]$ is the back ordered $A = [\alpha_i]$ set.

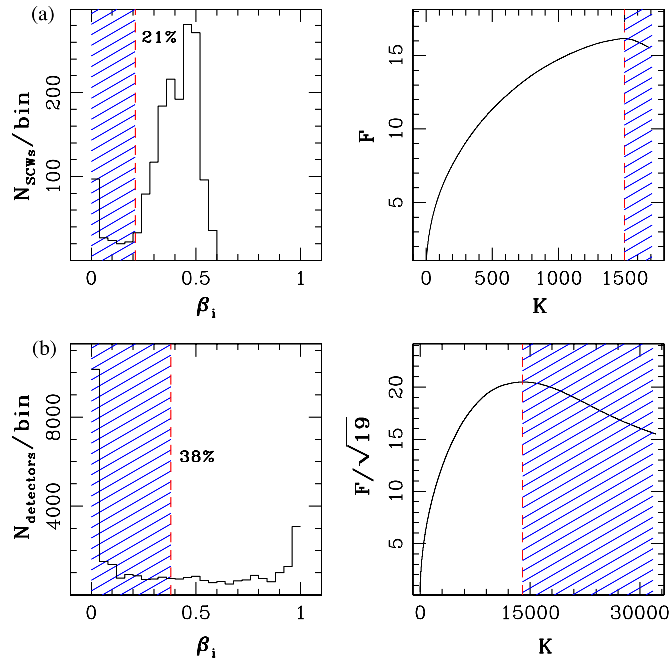

Figure 2. Left panels show the distribution of the number of SCWs (a) or the number of individual detectors (b) vs. their illumination fraction for our data set. The function $F(K)$ (see Equation (6)) is plotted on the rights panels for two cases: (a) the whole detector plane and (b) individual detectors. Shaded areas correspond to the data that should be excluded from the analysis. The function F in case (b) is renormalized to be in the same units as in case (a).

(A color version of this figure is available in the online journal.)

The speculations presented above could be easily extended to the case when we do not treat the whole detector plane (hereinafter referred to as case I) but each detector separately (case II). In the latter case, α_i is the illumination fraction of an individual detector and varies in the range 0–1, and M is the number of pointings times the number of the individual detectors (19 for SPI).

We have obtained the solution for our set of *INTEGRAL* observations for both cases as illustrated in Figure 2. To reach the maximum of the signal-to-noise ratio in case I, we should exclude from the analysis the pointings with an illumination fraction below 21%. In case II, we should use only those detectors that have an illumination fraction above 38%. Figure 2 shows that using individual detectors (case II) we obtain a $\simeq$ 30% improvement of the signal detection significance. In this paper dedicated to the timing analysis, we have implemented case II.

2.2. *Jodrell Bank Crab Pulsar Monthly Ephemeris*

For the folding of the Crab pulsar lightcurves, we have used the time solution derived from Jodrell Bank Crab Pulsar Monthly Ephemeris (Lyne et al. 1993) and the corresponding Crab Pulsar coordinates. The database is available through the World Wide Web (http://www.jb.man.ac.uk/pulsar/crab.html) and contains the dispersion-corrected time of arrival of the center of the main pulse (in TDB time system), the frequency and its first derivative and the range of validity. From this database we extracted the radio ephemerides covering the periods of the *INTEGRAL* observations. For each radio ephemeris record we took its two neighbors and calculated the second derivative of the frequencies so that the phases and frequencies given at the edge of the validity intervals and those deduced by extrapolation

Table 1
List of Observations Used in This Analysis

Rev. N^o	Observing Period UTC	Exp.[a] (ks)	Target[b]
	YEAR 2003		
0043	19.177–21.783 Feb.	164	CRAB
0044	22.163–24.772 Feb.	177	CRAB
0045	25.167–27.699 Feb.	162	CRAB
0102	14.623–17.218 Aug.	91	CRAB
0103	17.610–17.845 Aug.	22	CRAB
0124	19.430–22.031 Oct.	195	IC443
0125	22.422–25.023 Oct.	196	IC443
0126	25.414–28.015 Oct.	110	IC443
	YEAR 2004		
0170	5.122–7.302 Mar.	119	CRAB
0182	9.987–12.504 Apr.	197	IC443
0184	15.976–18.566 Apr.	222	IC443
0239	27.435–30.036 Sep.	187	CRAB
0247	21.363–23.964 Oct.	223	IC433
	YEAR 2005		
0300	28.910–31.504 Mar.	188	CRAB
0352	31.463–2.890 Aug./Sep.	200	A0535
0365	11.096–11.938 Oct.	59	CRAB
	YEAR 2006		
0422	28.729–31.198 Mar.	190	CRAB
0464	1.252–3.011 Aug.	60	Taurus
0483	28.711–29.627 Sep.	69	CRAB
	YEAR 2007		
0541	19.537–22.128 Mar.	213	CRAB
0605	27.016–28.927 Sep.	154	CRAB
	YEAR 2008		
0665	24.473–27.033 Mar.	194	CRAB
0666	27.463–30.022 Mar.	204	CRAB
0727	25.940–28.488 Sep.	197	CRAB
0728	28.932–1.499 Sep./Oct.	184	CRAB
	YEAR 2009		
0774	13.538–16.145 Feb.	196	CRAB

Notes.
[a] This value represents the total exposure of selected data.
[b] For the complete description of the observations see the ISOC site http://www.sciops.esa.int.

are consistent with each other better than 0.0001 in phase and 10^{-7} in frequency. The resulting ephemerides for the *INTEGRAL* observing periods are given in Table 2.

The main pulse arrival time in the monthly ephemeris is determined with an error around 60 μs that includes the uncertainty in the delay due to interstellar scattering $\sim$20 μs (owing to the dispersion measure uncertainty $\Delta\mathrm{DM} \sim 0.005$ pc cm^{-3}) as well as those arising from unknown instrumental effects $\sim$40 μs (see, e.g., Rots et al. 2004, and references there). While the first part can be treated as a statistical error that follows the Poisson statistic and decreases with the number of independent measurements, the second part should be treated as a systematic error that is always present in the measured values.

2.3. *RXTE*

The PCA instrument onboard the *RXTE* orbiting X-ray observatory consists of five identical proportional counters with a total area of 6500 cm^2, operating in the 2–60 keV energy range (Bradt et al. 1993). The accuracy of the *RXTE* clock in absolute time for our observing time interval (2003–2009 yr.) is better than 2 μs (see Rots et al. 2004, and references therein). Because of its large area and excellent time resolution and time accuracy, the instrument is sensitive enough to reconstruct a significant 400 bins phase curve of the Crab pulsar using an exposure of the order of 1 ks. We used Crab PCA observations that coincide in time (within two weeks) with any of our *INTEGRAL* observation and contain data in the Generic event mode format with time resolution better than 250 μs. For the fine clock correction and barycenter correction we used *faxbary* script from the FTOOLS package that calls the *axBary* code (see, e.g., the *RXTE* Guest Observer Facility). For the folding procedure we use the same routine and the same ephemerides as for SPI/*INTEGRAL*.

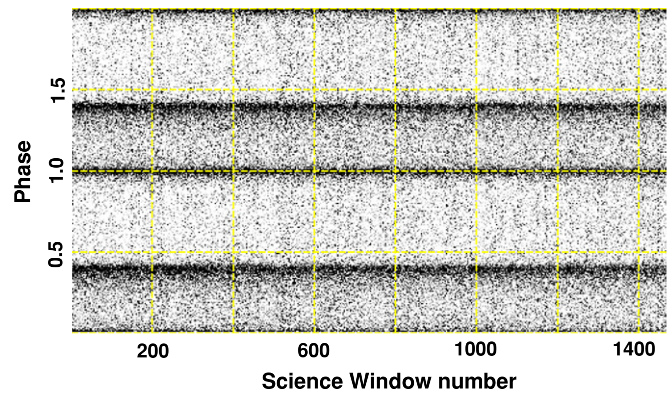

Figure 3. Science window by Science window folded curves in the 20–100 keV energy band. The folding procedure is based on ephemerides from Table 2. No $\Delta\Psi$ correction is applied (see the text).

(A color version of this figure is available in the online journal.)

3. SPI/*INTEGRAL* ANALYSIS AND RESULTS

To perform epoch folding analysis we ascribe to each detected photon the phase Ψ_t using the appropriate ephemeris from Table 2 and the following formula:

$$\Psi_t = \Psi_0 + f(t - t_0) + \frac{1}{2}(t - t_0)^2 \frac{df}{dt} + \frac{1}{6}(t - t_0)^3 \frac{d^2 f}{dt^2}, \quad (7)$$

where t_0, f, $\frac{df}{dt}$, $\frac{d^2 f}{dt^2}$ are the radio ephemerides valid for the moment "t" and $\Psi_0 \equiv 0$ (we want to work in the absolute phase, i.e., the main radio pulse is at phase 0.0). Then we can plot the phase values producing light curves with the requested resolution (here we use 400 bins per cycle). The middle of the zero bin is corresponding to the phase 0.0.

As a first step, to check our SPI data set for the presence of unknown "glitches" from the Crab pulsar or some instrumental artifacts (e.g., inaccuracy in the on-board to Universal Time conversion procedure) we folded separately each SCW lightcurve in the broad 20–100 keV energy band. The result of the dynamical folding is presented in Figure 3, where we see that the shape of the Crab phase histograms and absolute phases are very stable (the two peaks of the pulse are good tracers).

In order to determine the phase of the hard X-ray main pulse and interpulse more precisely and to study possible variations of these values in time we summed up the SCW folded curves for each revolution. The SPI pulse profile for the Crab pulsar in the 20–100 keV energy band for the exposure $\sim$100 ks is presented in Figure 4. To define the phase of the pulses, we fitted the data for each revolution with a composite model: a Gaussian function plus a constant background, in the phase intervals 0.98–1.01 and 1.38–1.41 for the main pulse and interpulse, respectively,

Table 2
The Crab Pulsar Ephemerides for the *INTEGRAL* Observations Listed in Table 1

Rev. N^o	T_{valid} (MJD), t_0^{Int} (MJD), t_0^{MP} (s)	f (Hz) df/dt (10^{-10} s^{-2}) d^2f/dt^2 (10^{-21} s^{-3})	Δt_0, μsec $\Delta\Psi$	Rev. N^o	T_{valid} (MJD), t_0^{Int} (MJD), t_0^{MP} (s)	f (Hz) df/dt (10^{-10} s^{-2}) d^2f/dt^2 (10^{-21} s^{-3})	Δt_0, μs $\Delta\Psi$
	52671–52699	29.8092705147	18		53431–53461	29.7847841837	−19
0043	52685	−3.7366060	0.0005	0300	53444	−3.7315793	−0.0006
	0.076659	9.0			0.033023	6.0	
	52671–52699	29.8092705147	−1		53584–53615	29.7798524524	36
0044	52685	−3.7366060	−0.0000	0352	53597	−3.7299236	0.0011
	0.076659	9.0			0.029626	9.0	
	52671–52699	29.8092705147	−69		53644–53675	29.7778867428	−24
0045	52685	−3.7366060	−0.0021	0365	53658	−3.7294045	−0.0007
	0.076659	9.0			0.022656	4.0	
	52852–52883	29.8034282349	8		53796–53826	29.7730221322	−19
0102	52866	−3.7350193	0.0002	0422	53809	−3.7278153	−0.0006
	0.018825	−1.0			0.005391	4.0	
	52852–52883	29.8034282349	31.0		53917–53948	29.7690932051	4
0103	52866	−3.7350193	−0.0009	0464	53931	−3.7267461	0.0001
	0.018825	−1.0			0.020193	15.0	
	52913–52944	29.8014598690	−11		53971–54009	29.7670971393	162
0124	52927	−3.7344076	−0.0003	0483	53993	−3.7264807	0.0048
	0.019997	3.0			0.011812	18.0	
	52913–52944	29.8014598690	−52		54160–54191	29.7612711958	−25
0125	52927	−3.7344076	−0.0016	0541	54174	−3.7245631	−0.0007
	0.019997	3.0			0.020652	5.0	
	52913–52944	29.8014598690	−31		54344–54374	29.7553516229	31
0126	52927	−3.7344076	−0.0009	0605	54358	−3.7225368	0.0009
	0.019997	3.0			0.010645	13.0	
	53068–53074	29.7969173441	−50.0		54526–54557	29.7494993041	−46.0
0170	53071	−3.7535080	−0.0015	0665	54540	−3.7206976	−0.0014
	0.010486	350.0			0.008472	13.0	
	53095–53105	29.7958809510	73		54526–54557	29.7494993041	−23
0182	53100	−3.7414057	0.0022	0666	54540	−3.7206976	−0.0007
	0.008622	200			0.008472	13.0	
	53105–53115	29.7955577865	−22		54710–54741	29.7435856030	54
0184	53110	−3.7392771	−0.0007	0727	54724	−3.7189687	0.0016
	0.024904	−100			0.013181	17.0	
	53255–53279	29.7906210263	40		54710–54741	29.7435856030	69
0239	53263	−3.7333983	0.0012	0728	54724	−3.7189687	0.0021
	0.021234	7.0			0.013181	17.0	
	53279–53311	29.7896533932	−48.0		54863–54892	29.7386704404	−23
0247	53293	−3.7329692	−0.0014	0774	54877	−371735.72	−0.0007
	0.101225	9.9			0.000804	14.9	

Note. We used the Crab Pulsar position given in Jodrell Bank: R.A. = 83$^\circ_.$633217 and decl. = 22$^\circ_.$014464 in the J2000 epoch.

and adopted the fitted position of the Gaussian centroid as the appropriate phase of the corresponding pulse. To make sure that the fit results are model independent, we fitted the data for the main pulse with two other models: Lorentzian—used in Rots et al. (2004; due to the lack of statistic for the one revolution timescale we could not apply the complete procedure of the peak-finding described in this paper) and Lorentzian plus constant—used in Kuiper et al. (2003). We found that all three models yield similar values, with dispersion not exceeding 0.0003 period (<10 μs).

The absolute phases of the main pulse and interpulse (with respect to the radio main pulse) together with the phase difference between them, as a function of the observation number, are shown in Figure 5. The distributions of Ψ_{P1} and Ψ_{P2} values are well consistent with normal distributions ($\Psi_{P2} - \Psi_{P1}$ is not a measured value but a combination of two independent functions). The mean value of the hard X-ray main pulse phase is 0.99182 ± 0.00046, thus, the pulse leads the radio main pulse by 8.18 ± 0.46 milliperiods or 275 ± 15 μs. Such quoted error does not include 40 μs coming from the uncertainty of the radio ephemeris. The average value of the two pulses separation is 0.3989 ± 0.0009 parts of the cycle. Note that this relative value is independent of any uncertainty in the radio timing ephemeris.

4. COMPARISON WITH PCA

For independent check of the hard X-ray results, we carried out the analogous analysis in the 2–20 keV energy band. We used the data of Crab observations with the PCA monitor quasisimultaneous with *INTEGRAL*. We used the same radio ephemeris and the same pulse definition procedure. The phase positions of the X-ray main pulse relative to the radio one for 79 PCA/*RXTE* observations are shown in the bottom panel of Figure 6, showing that also the main X-ray pulse leads the radio one. To determine the mean value of the time

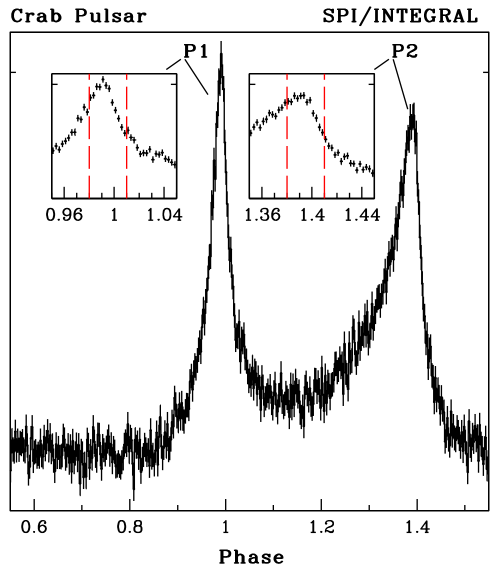

Figure 4. Crab phase histogram in the 20–100 keV energy band in absolute phase with the phase resolution of 0.0025. “1” corresponds to the phase of the main radio pulse. Inner panels magnify the main pulse and the interpulse peaks. Dashed vertical lines bound the intervals used for the fit procedure. The exposure is of the order of 100 ks.

(A color version of this figure is available in the online journal.)

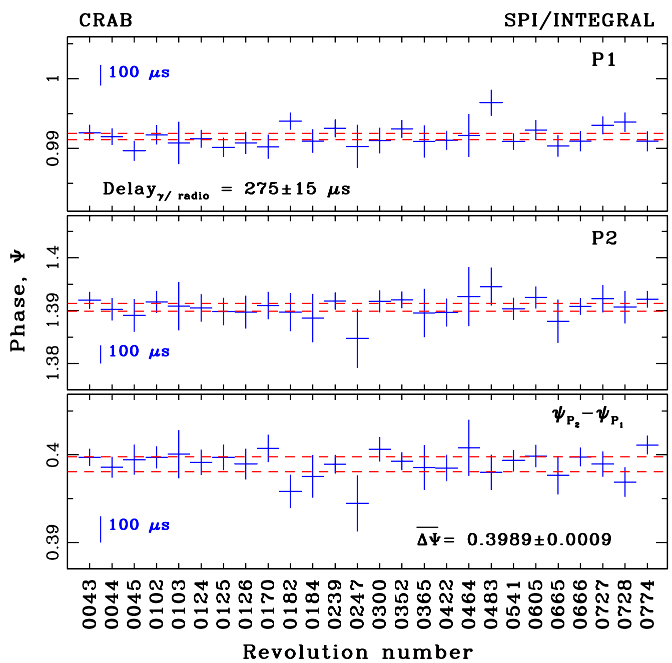

Figure 5. Best-fit values of the main pulse (P1), interpulse (P2) positions, and distance between them in the phase plane vs. the revolution number, in the 20–100 keV energy band. The horizontal dashed lines show the 1σ (statistical only) confidence intervals for the averaged values.

(A color version of this figure is available in the online journal.)

lag we approximated the PCA data with a constant and got 0.00933 ± 0.00016 in phase units or 310 ± 6 μs in time. Again we quote only statistical errors but we keep in mind the systematic $\sim$40 μs error that comes from the radio ephemeris uncertainties. Based on two measured time lags “X-ray/radio” and “hard X-ray/radio” we can conclude that the main X-ray pulse leads the hard X-ray main pulse by 35 ± 16 μs. This value differs only marginally from zero (we provided the 1σ error) even taking into account that in this case the radio error does not play a role since we used the same radio ephemerides

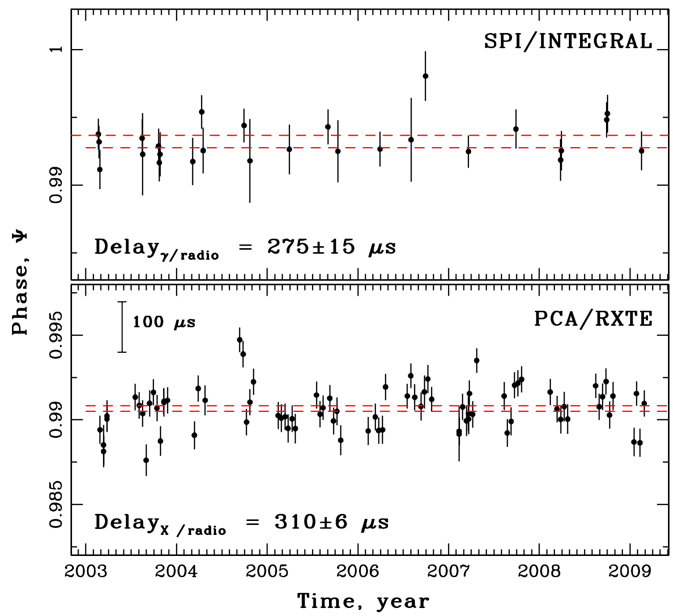

Figure 6. Main pulse maximum arrival phase in the 20–100 keV energy band with SPI/*INTEGRAL* (1 point by time interval order of 100 ks), and in the 2–20 keV energy band with PCA/*RXTE* (1 point—a few kiloseconds). The same radio ephemerides and fit procedure have been used. The horizontal dashed lines show the 1σ (statistical only) confidence intervals for the averaged values.

(A color version of this figure is available in the online journal.)

for both measurements. Another quantity that is independent of any uncertainty in the radio timing ephemerides is the phase difference between the main pulse and interpulse. From our set of PCA/*RXTE* observations, we got a value of 0.40016 ± 0.00028 that is in a good agreement with the result obtained in hard X-rays (0.3989 ± 0.0009, SPI/*INTEGRAL*).

5. RADIO DELAY EVOLUTION WITH ENERGY

We have measured accurately the delays of the main pulse arrival time in wide 2–20 keV (soft X-rays) and 20–100 keV (hard X-rays) energy bands with respect to the radio main pulse arrival time. The 310 ± 6 μs soft X-ray/radio delay derived in this paper based on the PCA data (Rots et al. 2004 provides even higher value 344 ± 40 μs) is marginally higher than the radio delay with respect to 275 ± 15 μs hard X-ray/radio delay measured with SPI. Both values are also slightly higher of the radio/optical delay of 255 ± 21 μs derived from S-Cam optical observations (Oosterbroek et al. 2008) and the 241 ± 29 μs radio/gamma one (>30 MeV, EGRET; Kuiper et al. 2003). To check whether these differences are real or not, we have made an additional analysis and investigated the behavior of the radio delay with energy. The radio delay evolution with energy has been observed in optical wavelength (Oosterbroek et al. 2008), that gave us an extra motivation. We have built folded curves in narrower energy bands. We split the 2–20 keV PCA energy band on three parts, while we used five energy channels to cover the 20–300 keV energy band for SPI data. We also added the High-Energy X-Ray Timing Experiment (HEXTE/*RXTE*) data in four energy bands covering the 20–250 keV energy range, allowing a direct crosschecking with SPI results. The position of the main peak has been determined as previously, from a fit with a composite model: a Gaussian function plus a constant background, in the phase interval 0.98–1.01. Figure 7 presents the evolution of the radio delay versus energy for the *RXTE* and SPI data, together with

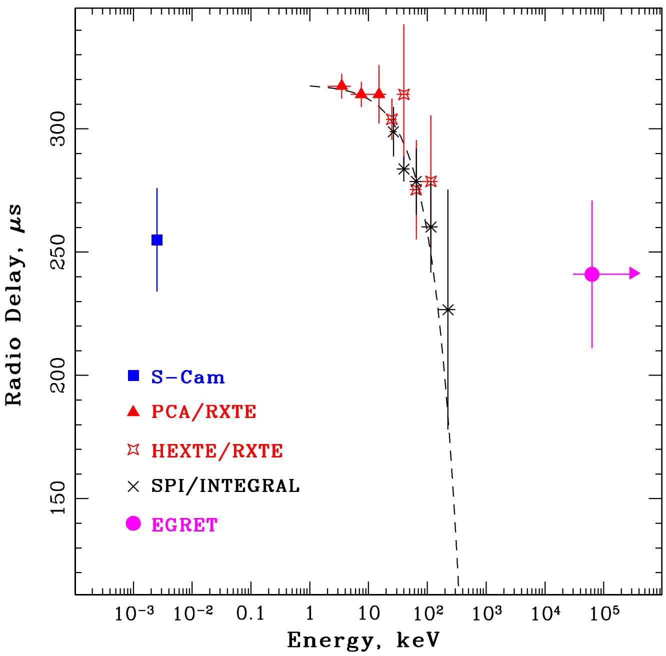

Figure 7. Radio delay in function of energy. The optical (S-Cam) and γ-ray (EGRET) points are from Oosterbroek et al. (2008) and Kuiper et al. (2003), respectively. The data of the *RXTE* instruments and SPI are from this work.

(A color version of this figure is available in the online journal.)

the optical and γ-rays points from Oosterbroek et al. (2008) and Kuiper et al. (2003). The decreasing trend of the radio delay with energy in the (2–300 keV) energy domain supports the reality of the delay measured between the soft X- and hard X-ray main peaks, even though the individual error bars are large. When modeling this decrease by a simple linear law (dashed line in Figure 7) we find that the radio delay decreases with a rate of $\sim 0.6 \pm 0.2$ μs keV^{-1}. The obtained Chi2 of 7.1 for 10 dof compared to the value of 42.4 for 11 dof for a constant model corresponds to a probability of 3.5×10^{-5} that its improvement is by chance.

6. DISCUSSION AND CONCLUSIONS

We have investigated the pulse profile of the Crab pulsar between 2 and 300 keV with PCA/*RXTE* instrument and SPI/*INTEGRAL* telescope. We found the strong indication that in this energy range the radio delay is significantly decreasing with energy. The simplest explanation of such a behavior is that the X-ray/$\gamma_{\rm soft}$-ray emission originates in a region extended along the open magnetic field lines, with softer photons originating at higher altitudes while the time offsets represent simply the path-length differences. In this case, the time delay determines the characteristic azimuthal size of the emitting area as 54 ± 18 km.

It is clear that the radio delay cannot decrease linearly through the full gamma rays range, since the EGRET point imposes a positive value. Moreover, contrary to we observe above 2 keV, the radio delay increases between optical and X-rays. It is interesting to note that the X-ray delay is consistent with the rate of -5.9 ± 1.9 μs/1000 Å derived from the 3920 to 8230 Å optical waveband by Oosterbroek et al. (2008).

Even thought the dependence of the main pulse phase position on energy is complex, we can explain it with a rather simple scheme, where the pulsed emission consists of the superposition of two independent components having different phase distributions and energy spectra. Indeed, such an analytical model has been introduced by Massaro et al. (2000) to interpret the BeppoSAX data in the 0.1–300 keV energy band (see also improvements Massaro et al. 2006; Campana et al. 2009). In the optical up to γ-ray domain, this model includes an "optical," C_o and an "X-ray," C_x. The fractional part of the C_x component increases in the main pulse with increasing energy from 1 keV up to a 1 MeV, then decreases up to $\sim$10 MeV energy but is negligible below 1 keV and above 10 MeV. C_x/C_o ratio behavior following the same law as the Bridge/P1 ratio presented in Kuiper et al. (2001). Thereby, in the X-ray band, the C_x component shifts the maximum of the pulse I ($C_x + C_o$) emission toward the radio maximum on the phase plane. It explains that the radio delay decreases with energy in X-rays, while it keeps identical values in the optical and γ-ray wavebands where the C_x component is negligible. Considering that the values of the radio delay are nearly the same in the optical wavelengths and γ-rays, where C_o largely dominates over C_x, we can suggest that the C_o component corresponds to a single emission mechanism and emission location from optical to γ-rays. In this case, the $\sim$250 μs radio delay indicates that the radio emission is produced in a region located closer from the Neutron Star by $\sim$75 km than the C_o production site. On the other hand, the C_x component could be unrelated to the C_o one, with a different origin and/or source location. In this case, the source behavior in X-rays would result from a superposition of (at least) two independent components and the measured values of the radio delay in this energy band would not have any direct physical explanation.

We are grateful to Professor Hermsen, Dr. Kuiper, Dr. Rots, and Dr. Revnivtsev for the very helpful technical notes and discussion. We thank the *INTEGRAL* helpdesk team (especially Dr. Turler, ISDC) and Dr. Southworth (ESOC) for productive discussion of the *INTEGRAL* timing facilities and prompt correction of newly discovered problems. We acknowledge HEASARC at NASA/Goddard Space Flight Center for maintaining its online archive service which provided the *RXTE* data used in this paper. This research has been supported by CNES.

REFERENCES

Alenia Spazio 2002, *INTEGRAL* End-to-End Timing Test Report, INT-RP-AI-0227 (European Space Agency)
Attié, D., et al. 2003, A&A, 411, L71
Bradt, H. V., Rothschild, R. E., & Swank, J. H. 1993, A&AS, 97, 355
Bradt, H., et al. 1969, Nature, 222, 728
Brandt, S., et al. 2003, A&A, 411, L433
Campana, R., Massaro, E., Mineo, T., & Cusumano, G. 2009, A&A, 499, 847
Courvoisier, T. J.-L., et al. 2003, A&A, 411, L53
Dean, A. J., et al. 2008, Science, 321, 1183
Eismont, N., et al. 2003, A&A, 411, L37
Fritz, G., et al. 1969, Science, 164, 709
Kuiper, L., et al. 2001, A&A, 378, 918
Kuiper, L., et al. 2003, A&A, 411, L31
Kurfess, J. D. 1971, ApJ, 168, L39
Leahy, D. A., et al. 1983, ApJ, 266, 160
Lund, N., et al. 2003, A&A, 411, L231
Lyne, A. G., Pritchard, R. S., & Graham-Smith, F. 1993, MNRAS, 265, 1003
Mas-Hesse, M., et al. 2003, A&A, 411, L261
Masnou, J. L., et al. 1994, A&A, 290, 503
Massaro, E., Campana, R., Cusumano, G., & Mineo, T. 2006, A&A, 459, 859
Massaro, E., Cusumano, G., Litterio, M., & Mineo, T. 2000, A&A, 361, 695
Moffett, D. A., & Hankins, T. H. 1996, ApJ, 468, 779
Nolan, P. L., et al. 1993, ApJ, 409, 697
Oosterbroek, T., et al. 2008, A&A, 488, 271
Pravdo, S. H., Angelini, L., & Harding, A. K. 1997, ApJ, 491, 808
Roques, J. P., et al. 2003, A&A, 411, L91
Rots, A. H., Jahoda, K., & Lyne, A. G. 2004, ApJ, 605, L129

The MAGIC Collaboration 2008, Science, 322, 1221
Thompson, D. J., et al. 1977, ApJ, 213, 252
Ubertini, P., et al. 2003, A&A, 411, L131
Vedrenne, G., et al. 2003, A&A, 411, L63
Walter, R., et al. 2003, A&A, 411, L25
White, R. S., Sweeney, W., Tumer, T., & Zych, A. 1985, A&A, 299, L23
Wills, R. D., et al. 1982, Nature, 296, 723
Winkler, C., et al. 2003, A&A, 411, L1